AFRL-AFOSR-VA-TR-2016-0150

Dynamic High-Pressure Behavior of Geological Materials

Naresh Thadhani
GEORGIA TECH RESEARCH CORPORATION

04/01/2016
Final Report

Air Force Research Laboratory
AF Office Of Scientific Research (AFOSR)/ RTA1
Arlington, Virginia 22203
Air Force Materiel Command

REPORT DOCUMENTATION PAGE

Form Approved
OMB No. 0704-0188

1. REPORT DATE *(DD-MM-YYYY)*	2. REPORT TYPE	3. DATES COVERED *(From - To)*
08-04-2016	Final Performance	01-04-2012 to 31-12-2015

4. TITLE AND SUBTITLE
Dynamic High-Pressure Behavior of Hierarchical Heterogeneous Geological Materials

5a. CONTRACT NUMBER

5b. GRANT NUMBER
FA9550-12-1-0128

5c. PROGRAM ELEMENT NUMBER
61102F

6. AUTHOR(S)
Naresh Thadhani

5d. PROJECT NUMBER

5e. TASK NUMBER

5f. WORK UNIT NUMBER

7. PERFORMING ORGANIZATION NAME(S) AND ADDRESS(ES)
GEORGIA TECH RESEARCH CORPORATION
505 10TH ST NW
ATLANTA, GA 30318-5775 US

8. PERFORMING ORGANIZATION REPORT NUMBER

9. SPONSORING/MONITORING AGENCY NAME(S) AND ADDRESS(ES)
AF Office of Scientific Research
875 N. Randolph St. Room 3112
Arlington, VA 22203

10. SPONSOR/MONITOR'S ACRONYM(S)
AFRL/AFOSR RTA1

11. SPONSOR/MONITOR'S REPORT NUMBER(S)

12. DISTRIBUTION/AVAILABILITY STATEMENT
A DISTRIBUTION UNLIMITED: PB Public Release

13. SUPPLEMENTARY NOTES

14. ABSTRACT

The characteristics of shock-wave propagation in high purity sand of fine (75-150 m) and coarse (425-500 m) particle sizes in dry stat at ~65%
theoretical density, and water-saturated with 35% void space filled with water, were collaboratively investigated, via controlled uniaxial-strain
experiments and meso-scale modelling using CTH. The meso-scale features of the sand were resolved by explicitly incorpoprating 3D grains and
void space into the computational domain. The method involved characterizing the structure and configuration of sand, as a model granular
geological material, and explicitly tracking the effects of evolving material heterogeneities and their interactions with shock waves. It was observed
that both dry and wet sand follow linear trends, with little difference in overall response between the two sizes of sand particles. Accounting for
different strength values into CTH, provided upper and lower bounds to the experimental data. Results suggest effects of microkinetic energy,
chipping on grain surfaces, and plastic deformation dominating the experimental response. These are difficult to incorporate in the simulation
models. Experiments also reveal significant reduction in bulk wave speeds, which requires incorporation of multiple mechanisms in simulations

15. SUBJECT TERMS
High-rate Deformation, Heterogeneous Materials, Shock Physics

Standard Form 298 (Rev. 8/98)
Prescribed by ANSI Std. Z39.18

16. SECURITY CLASSIFICATION OF:			17. LIMITATION OF ABSTRACT	18. NUMBER OF PAGES	19a. NAME OF RESPONSIBLE PERSON
a. REPORT	b. ABSTRACT	c. THIS PAGE			Naresh Thadhani
Unclassified	Unclassified	Unclassified	UU		19b. TELEPHONE NUMBER *(Include area code)* 404-894-2651

Standard Form 298 (Rev. 8/98)
Prescribed by ANSI Std. Z39.18

Dynamic High-Pressure Behavior of Hierarchical Heterogeneous Geological Materials

Naresh Thadhani, Greg Kennedy, and Sunil Dwivedi
School of Materials Science and Engineering, 771 Ferst Drive,
Georgia Institute of Technology, Atlanta, GA 30332-0245

Sarah Stewart and Dylan Spaulding
Dept. Earth and Planetary Sciences, University of California at Davis
One Shields Avenue, Davis, CA 95616

Markos Hankin
Department of Earth and Planetary Sciences, Harvard University,
20 Oxford Street, Cambridge MA 02138

John Borg, Jeff Lajeunesse, and Peter Sable
Department of Mechanical Engineeing, Marquette University
1515 W. Wisconsin Ave., Milwaukee, WI 53233

AFOSR Award No: FA9550-12-1-0128

Final Report

March 30, 2016

ABSTRACT

The characteristics of shock-wave propagation in high purity sand of fine (75-150 μm) and coarse (425-500 μm) particle sizes in dry conditions at ~65% theoretical density, and water-saturated conditions with 35% void space filled with water, were collaboratively investigated, via controlled uniaxial-strain experiments and meso-scale modelling using CTH. The meso-scale features of the sand were resolved by explicitly incorpoprating 3D grains and void space into the computational domain. The methodology involved characterizing the structure and configuration of sand, as a model granular geological material, and explicitly tracking the effects of evolving material heterogeneities and their interactions with shock waves. It was observed that both dry and wet sand follow linear trends, with little difference in overall response between the two sizes of sand particles. Accounting for different strength values into CTH, provided upper and lower bounds to the experimental data. Results suggest effects of microkinetic energy, chipping on grain surfaces, and plastic deformation dominating the experimental response. These are difficult to incorporate in the simulation models. Experiments also reveal significant reduction in bulk wave speeds, which requires incorporation of multiple mechanisms in the simulations.

OUTLINE

1. **BACKGROUND**

The dynamic behavior of heterogeneous materials used as colliding objects under conditions of high pressure and high-strain-rate (10^3 to 10^9 s^{-1}) loading, is complicated by the inability to monitor the material response and interactions of shock waves with heterogeneities, at the time scale of the interaction and the length scales of the initial or evolving heterogeneities. Modeling and predicting the behavior of heterogeneous materials is also challenging because of the effects of multiple constituents, phases, inter-phase boundaries; distributions in shock states; as well as the structural evolutions which can result in strain-localization. Recent advances in experimental and multi-scale modeling and simulation have in fact, shown the need for treating all materials as heterogeneous, in order to gain full insight into their response under high-pressure shock-compression and high-strain-rate behaviors. The heterogeneities inherent in the case of geological or earth materials (such as rocks and soil), as well as structurally-engineered or synthetic monolithic and composite materials, have significant influence on the high-pressure and high-strain-rate behaviors. The interactions of shock waves with inclusions, second phase particles/additives, phase/grain boundaries, as well as evolving effects such as texture, phase changes, and failure under inertial confinement, complicates their incorporation in modeling and are also difficult to isolate in experiments. Even water present in soils can exhibit analogous effects due to phase changes and ice formation under shock loading. Understanding the material response under the combined effects of the hierarchical scale of heterogeneities, as well as those evolving and resulting in anisotropy, temperature increases and localized softening, phase changes, inter- and intra-material fracture, friction, etc., remains a challenge.

The effects of shock wave interactions with inherent or evolving heterogeneities in materials often consist of (a) elastic-inelastic deformation of individual constituents, grains, inclusions, second phase additives, etc., whose properties may be varying due to random orientations or due to dissimilar material characteristics, (b) inter-grain or inter-phase or even free-surface interactions which may have finite strengths varying randomly or generating sliding and frictional effects, (c) temperature rise with heat conduction resulting in coupled thermal-stress phenomena, and (d) grain/phase boundary de-cohesion leading to fracture, crack propagation, and even fragmentation, phase changes, etc. A significant amount of numerical and experimental work exists on individual phenomenon, at homogenized continuum scales. However, experimental approaches that capture the effects at the spatial scale of the heterogeneities and time scales of the interactions are still lacking. Likewise, comprehensive modeling and simulation approaches that incorporate the shock wave interactions with heterogeneities, while encompassing these phenomena and without leaving out the predominant role of one or the absence of other phenomenon are not yet available.

Geological materials including soils and rocks are examples of heterogeneous materials containing discrete heterogeneities of vastly different impedances. The shock compression response of solids, including granular materials, is typically determined using uniaxial strain loading employing planar-parallel plate-impact experiments. The peak stress, particle velocity, or shock velocity, are measured using point diagnostics employing either stress gauges or interferometry methods, to generate the equation-of-state (EoS).

The limited amount of EoS data available for soils and other granular geological materials demonstrate the challenges in performing such experimental measurements. The dynamic response of granular materials obtained as pressure-volume or shock versus particle velocity trends is strongly dependent on specific mineral assemblages, initial density, and water content [1-5]. Hence, a knowledge of the unloading behavior (release isentropes) is also often necessary to determine their high-pressure high-strain-rate response. Figure 1 shows an example of the pressure-volume shock compressibility and release isentropes for wet and dry soil of initial density 1.55 g/cm^3. It can be seen that the porous dry soil is much more compressible than the water-saturated soil. The release isentropes show irreversible compaction of the dry soil at modest shock pressures (~8 GPa), whereas the wet soil is much less compressible. At higher pressures (~28 GPa or 280 kbars), the water-saturated soil shows significant volume expansion upon release that is driven by water vaporization. Correspondingly, the final free-surface particle velocities upon release from ~28 GPa is higher for wet soil (9 km/s) than dry soil (7 km/s). These data illustrate the importance of understanding and characterizing the role of constituents (such as that of water) on dynamic compression of heterogeneous materials such as soils. In addition, current numerical techniques are unable to predict *a priori* the dynamic response of soils under the wide range of heterogeneities, arising from those based on conditions in the field.

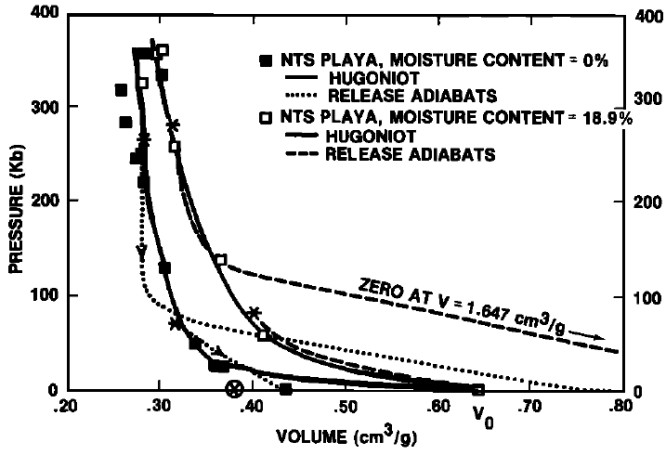

Figure 1. Shock Hugoniots (solid curves) and release isentropes (dotted and dashed curves) for wet and dry soil of 1.55 g/cm^3 initial density illustrating differences in compressibility [1].

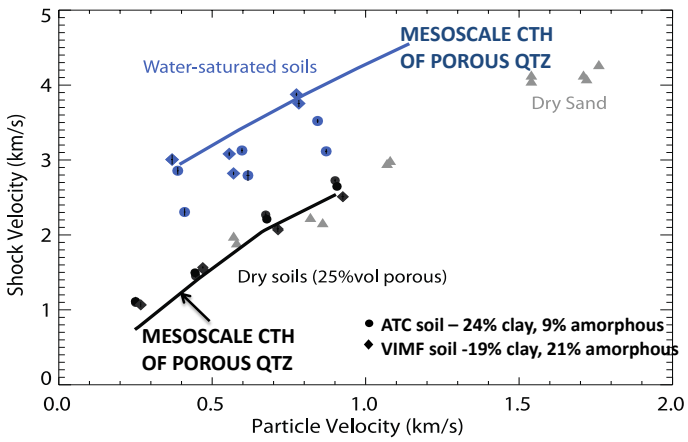

Figure 2. Measured U_s-U_p data for dry and water-saturated soils correlated with CTH simulations show better correlation with the linear trends for dry soil, but over-predicting of simulated shock velocities for wet soil which also shows more scatter.

Figure 2 shows another example illustrating the shock versus particle velocity equation-of-state of sand providing clear evidence of the effects of porosity and moisture content on the measured response

from prior work performed at Harvard. The equation-of-state treats granular materials (sand) as homogeneous (continuum) materials. Hence, it does not capture the mesoscale effects of heterogeneities associated with variations in particle morphology or particle size distribution, or particle-particle interactions, and nor the effects of phase transitions, fragmentation, etc. Obtaining the mesoscale heterogeneous response of granular materials therefore requires multi-scale simulations that account for inherent in homogeneities, such as with the use of actual or simulated microstructures. It is also necessary to have the understanding of well-characterized effects of particle interactions with friction, energy dissipation, heat generation and conduction, damage and/or fracture, and their coupling, through controlled time-resolved experiments with systematic variations in scale and type of heterogeneities in the granular materials investigated.

The dynamic response of geological granular materials such as soils is even more difficult to predict because of the multiple aspects of their heterogeneous nature. Soils have a mixed composition that generally includes four components: minerals (inorganic materials), organic materials, water, and air (porosity). The relative proportions of these four components vary with soil type and climatic conditions. Second, the particle sizes are heterogeneous. The texture of soil is determined by the size of the particles and is classified as clay (<0.002 mm), silt (0.002-0.02 mm), sand (0.02-2 mm), or gravel (>2mm), based on the International Society of Soil Science scale. A roughly equal mixture of clay, silt and sand sized particles is called loam (a textural class). Third, the water component is temporally and spatially variable and may intially be in liquid or solid state, and transition to solid, liquid or vapor states, which result in significantly different mechanical and thermodynamic behavior. Finally, natural soil is a layered medium that may also contain biota or other structures that affect its mechanical response. Because of the widely varying properties of natural soils, the most efficient means for understanding the dynamic response of soil in a particular region of interest has been to measure the properties of direct samples. However, the present body of data on soils does not provide sufficient validation of modeling efforts that attempt to understand how varying individual properties of a soil sample will affect its dynamic response, as has been illustrated in recent studies by Brown et al [4].

Soils containing mixtures of sand and water, or ice, bring also another level of heterogeneity, not only because of the vast differences in the shock impedance of the constituents, but also because of phase transitions that can occur in one or more constituents. In such cases, due to multiple wave interactions between the components, the thermodynamic loading path may not be expected to be along a single-shock Rayleigh line (but rather along a quasi-isentrope) and the final state may not be on the Hugoniot of the mixture [6]. The Harvard group led by Stewart [7] has extensively studied icy and porous geological materials. In this prior work, they obtained the Hugoniot states for a 60:40 volumetric mixture of ice and sand [8], to determine the partitioning of shock energy between the two components with strong differences in impedance. They observed that ice-sand mixture reaches a nearly ideal principal Hugoniot state, i.e., the sand and ice were under the same pressure at their respective compressed volumes (as shown in Figure 1). Furthermore, based on pyrometry measurements, they found that the peak temperature of the water was determined by its Hugoniot state, with the time

scale for thermal equilibration between the components depending on the length scales and conductivities of the materials. The shock temperature experiments also illuminated the role of phase changes during decompression of shocked water [7]. They found that when a supercritical fluid (water) unloads from the shock state, it quickly expands to a state on the saturation vapor curve (the liquid-vapor boundary between the ice Ih-liquid-vapor triple point at 273 K and 0.0006 MPa and the critical point at 647 K and 22 MPa). In order to continue unloading, the hot fluid must expand significantly through the production of vapor which takes time and depends on the surrounding pressure conditions (e.g., confined or unconfined). The unloading process determines the final particle velocities achieved by release of the supercritical water. In the ice-sand mixture, there is negligible volume change in the sand components; however, above the modest shock pressures required for vaporization upon release, the water component undergoes significant volume expansion. The volume expansion is accompanied by large particle velocities in the water/vapor component which accelerates the sand component. Hence, understanding the unloading process, including phase changes, in water-rich soils is paramount for determining their high-pressure response, which makes it obvious that the thermodynamic complexities of high-pressure effects in heterogeneous materials such as soil-water mixtures need to be better explained.

While soils and soil-water mixtures represent an example of a complex heterogeneous materials system, developing an understanding of the high-pressure shock compression response of loose dry granular material such as sand or metal (or ceramic) powders, even with regards to correlating model predictions of their bulk behavior with experimentally measured trends, has been challenging. For example, Figure 3 (a,b) compares the experimentally measured average longitudinal stress (Hugoniot) as a function of density for tungsten carbide

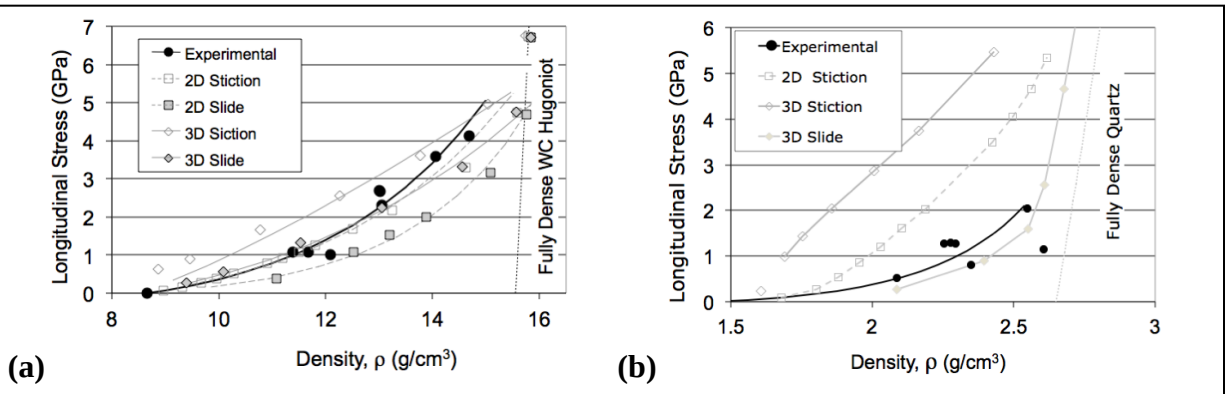

Figure 3. Comparison of experimentally measured and simulated Hugoniot for powder compacts of (a) tungsten carbide and (b) sand. Various configurations illustrate effects of varying grain-on-grain friction behavior: stiction versus sliding.

powder and sand, with predictions based on meso-scale simulations incorporating grain-grain interactions [9,10]. It can be seen that the response can be sensitive to not only the dimensionality of the simulation but also the grain-on-grain contact laws. Comparing results for tungsten carbide with sand, it also illustrates that although two-dimensional stiction simulations are equivalent to three-dimensional sliding simulations for tungsten carbide, they

are not equivalent for sand. Hence, it cannot be *a prior* determined which dimensionality and to what degree friction is necessary in order to predict the system response. Thus, there is much to be learned by investigating even simple granular systems subjected to uni-axial strain loading. The work performed in this project, therefore concentrated on high purity sand of controlled particle size distribution, in both dry and wet conditions.

2. CHARACTERISTICS OF SAND INVESTIGATED

We acquired a large batch of Oklahoma #1 pure sand from US Silica mine in Mill Creek, OK. The sand was sieved to obtain various ranges of particle size distributions, as shown the SEM images in Figure 4. The sand particles were of a rounded particle shape, and their controlled size enabled a better correlation with mesoscale simulations such that the simulated response and predicted behavior can be directly compared with measurements, while accounting for interparticle effects including friction, fracture, phase changes, under dry and water-saturated states. In order to isolate and maximize the role of particle size effects, the sand was sieved to retrieve and collect enough amounts of two extremes of sand partciles. Figure 5 shows the SEM images of the two extremes of the sand particles of sizes including 75-150 µm (hereby referred to as 'Fine' sand) and 425-500 µm (hereby referred to as 'Coarse' sand. It can be seen that the rounded sand particles appear to be fairly uniform in size distribution. Additionally, the coarser particles appear to be more transparent than the fine sand particles.

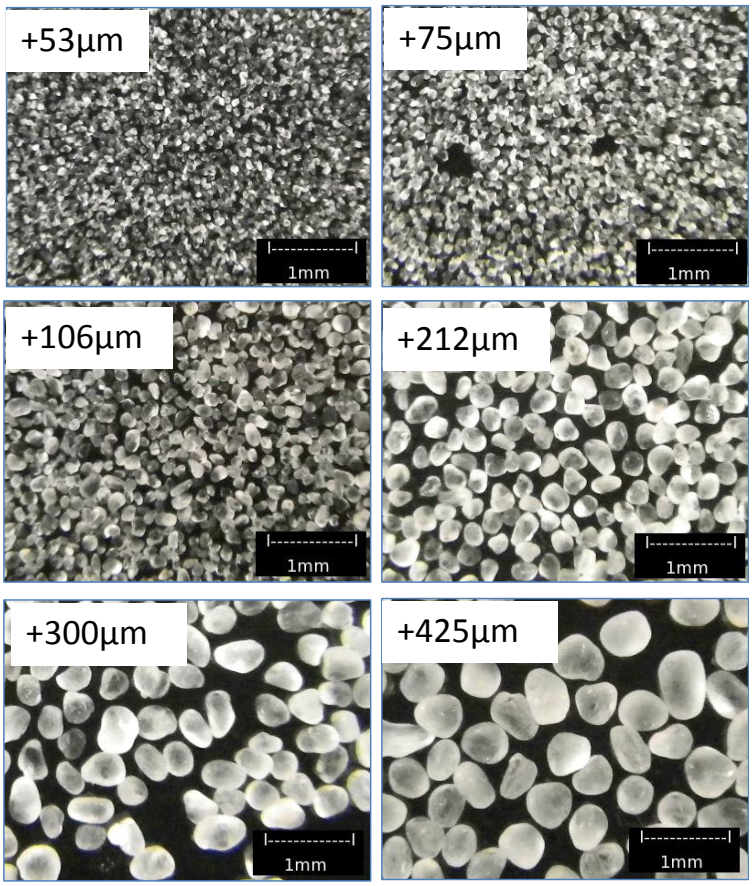

Figure 4. SEM images of various sieved particles of Oklahoma #1 pure sand.

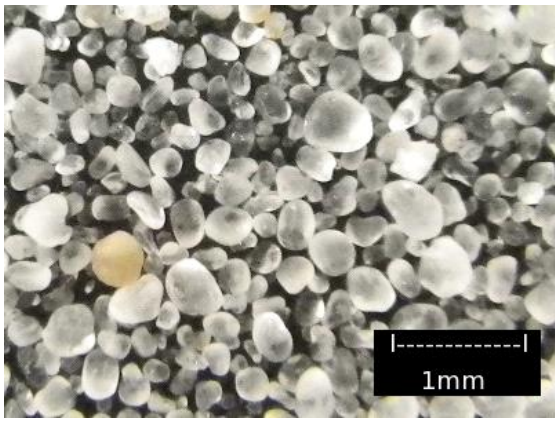

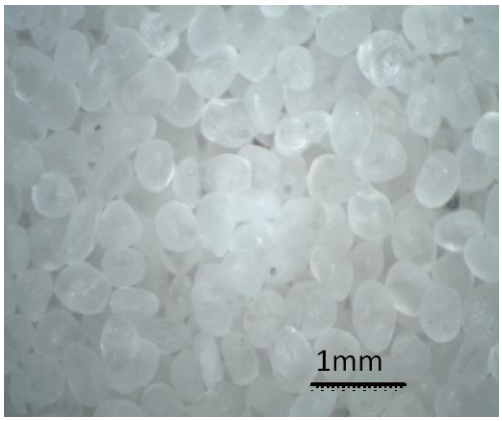

Figure 5. SEM images of two extremes of particle sizes of pure sand, 75-150 µm (fine) and 425-500 µm (coarse) used for shock compression experiments performed in present work.

3. UNIAXIAL-STRAIN SHOCK-COMPRESSION EXPERIMENTS ON SAND

In the present work, uniaxial-strain shock-compression experiments were performed on the same bacthes of sand of two extremes of particle sizes, 75-150 µm (fine) and 425-500 µm (coarse), shown in Figure 5. Gas gun facilities at Georgia Tech, AFRL Eglin AFB, and Harvard University were used employing similar configurations at impact velocities in the range of 0.2 to 2.0 km/s. Hence, the size of the coarse sand was selected such that the largest diameter would have a thickness equivalent to a minimum of 10 grains, perfectly stacked, for a sample height of 4.5 to 5mm. This sample thickness was selected to be consistent between the testing facilities, with the smallest diameter gun controlling the area of plane strain in the experiments. The gun with the smallest barrel diameter of 40 mm was required for testing at velocities greater than 1km/s and the sample was chosen to be 1/10 the diameter of the gun barrell.

3.1 Dry Sand Experiment Set-up used at Georgia Tech

Uniaxial-strain plate-impact experiments using the 80-mm dimeter single stage gas gun at Georgia Tech were performed on the fine and coarse size distributions of silica sand, SiO_2, in the dry condition. Figure 6 shows a schematic of the dry sand experiment set-up used. The sand was packed in a copper capsule with a 6.3mm copper driver plate glued to a 44.4mm internal diameter copper ring. The amount of sand was carefully measured to provide the desired density when the sand was tamped to the thickness of the given volume of the copper capsule. The sand was poured into the capsule and a 1kg steel plug of same diameter as copper capsule was placed on top of the sand for tamping. The tamping was a grain rearranging process achieved by vibrating the entire assembly with a Vortex Genie 2 shaker (from Scientific Industries), while the steel tamper was held loosely against the sand. Without this vibrating process, the grains would easily lock up at less than the desired density. Tamping of fine grains was more difficult than for coarse grains, but densities of ~1.72g/cm^3 or 65% of TMD were achieved. The steel plunger was removed after the required height was achieved from the

vibration and an 18 mm thick PMMA backer was placed into the capsule. The sample often required a slight vibration treatment to achieve the same density after the placement of the PMMA backer due to particles moving around when the tamper was extracted. The majority of the rearrangement of the grains was done with the steel tamper to prevent damage to the PVDF gauge package on the face of the PMMA backer.

A PVDF gauge package was attached to the downrange face of the copper driver plate and the uprange face of the PMMA window/backer material. The PVDF gauge package consisted of a 25µm PVDF gauge sandwiched between two 25µm FEP copolymer layers attached to the copper driver plate. The total package thickness with thin-film epoxy on all bonding surfaces was approximately 100µm. The same technique was used on the uprange face of the backer material, except a 25µm aluminum layer was previously bonded to the same surface of the PMMA window for reflectivity of the VISAR and PVD velocity measurement systems. Once the sample was at the proper thickness and density, the capsule was sealed with epoxy around the PMMA and copper ring joint. The entire assembly was then placed into a PMMA mounting ring that would later be attached to the muzzle of the 80 mm gas gun. Time of arrival, TOA, pins were placed around the sample to measure the arrival time of the flyer, as well as the tilt during the impact event. The overall set-up is illustrated in the schematic shown in Figure 6, and Figure 7 shows a photograph of the sample mounted onto the Georgia Tech 80 mm gas gun. along with the associated diagnostics.

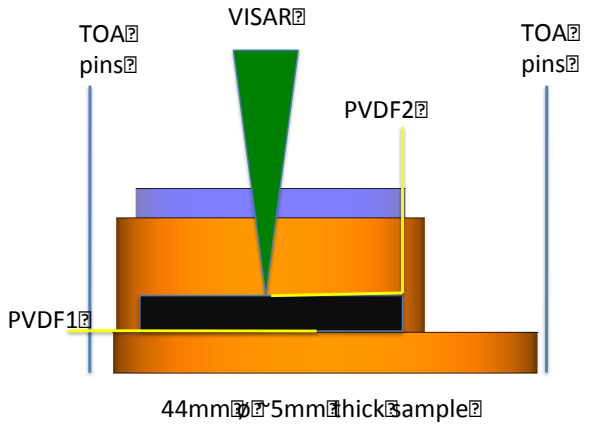

Figure 6. Schematic of set-up used with GT 80-mm gas-gun; sand sampleis pressed in copper capsule, backed with PMMA. The instrumentation includes two PVDF stress gauges, VISAR, and ToA shorting pins.

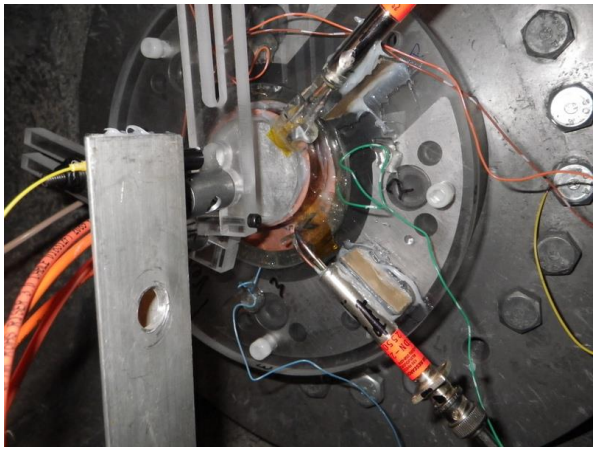

Figure 7. Photograph of sample mounted on GT 80mm gas gun along with diagnostics.

A copper flyer plate was attached to the front of an 80 mm diameter aluminum projectile of a mass required to achieve the required velocity for impact in the gas gun. An air gap was placed at the rear of the copper to prevent partial unloading of the copper flyer before full compaction of the sand. The copper flyer plates were 6.3mm thick in the higher velocity range but a 9.1mm thick flyer was required for the low velocity experiment, 412m/s, to prevent the release from rear surface of the flyer plate from arriving before full compression of the silica sand. Projectile velocity was

measured with a series of 4 shorting pins of precisely measured spacings contacting the periphery of the projectile face prior to impact. Interface particle velocity measurements were made with VISAR in all experiments. PVDF gauge signals were used at the copper sand interface to determine the wave arrival time while the propagated wave of the PVDF gauges yielded unreliable values due to the destruction of the gauge from the long rise times and extensive particle motions. The propagated PVDF gauge measurements however detected early elastic waves or force chains but their magnitude could not be determined due to shearing of the 25 µm thick PVDF film. Shock velocities were determined from the time between input PVDF gauge, typically <10ns rise time and VISAR particle velocity record from the thin reflective aluminum layer at the sand PMMA interface.

3.2 Set-up used at AFRL-Eglin

The setup for AFRL Eglin AFB was slightly modified from the Georgia Tech version due to the projectile velocity measurement system available at AFRL which reduces the diameter of the sample. Figure 8 shows the schematic and Figure 9 shows a photograph of the modified capsule geometry used with the powder gun at AFRL Eglin facility. The sample diameter was reduced to 41.3 mm due to the requirement of adding PDV probes around the sample diameter to observe the velocity of the incoming projectile. The samples were packed with the same coarse and fine sand designations for the similar thickness and density in the copper capsule assembly, as in the case of the Georgia Tech set-up and then dropped into aluminum target holding fixture used with the gun facility. The input PVDF gauges end up being destroyed by the aluminum impacted by the projectile before recording any usable signals. The breakout time of the copper driver was calculated from the thickness of the copper driver and the calculated shock velocity of the symmetric copper flyer driver impact. The breakout time and the interface particle velocity recorded by the VISAR probe were used to calculate the shock velocity in the known thickness of the silica sand.The projectile consisted of an aluminum cup with a lip, for an air

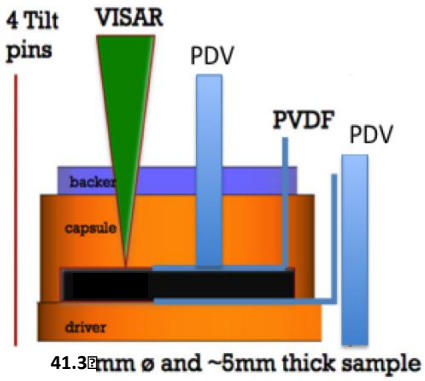

Figure 8. Schematic of modified capsule geometry used at AFRL.

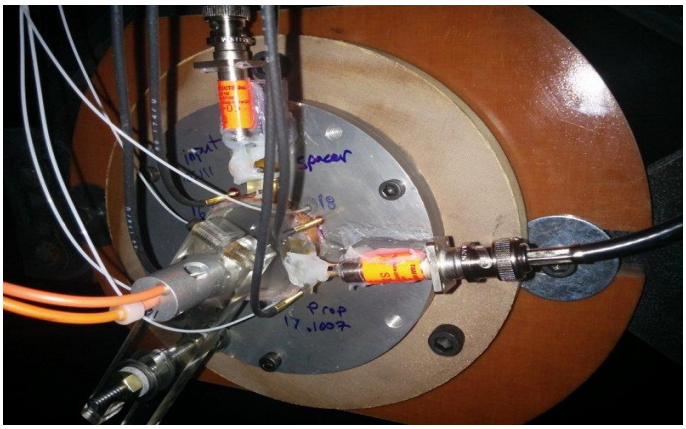

Figure 9. Photograph of the sample mounted to the AFRL Eglin target holding fixture.

gap, machined to support the 6.3mm thick 48 mm diameter flyer plate. That aluminum cup assembly was mounted in a phenolic tube with a flared plastic endcap as was typical for use in the powder gun facility. The velocity of the projectile was measured with three PDV probes around the periphery of the face of the flyer plate before impact. The aluminum target ring was aligned to the gun by mounting to a fixture that was aligned to the gun axis using a calibrated optical flat on a plug inserted into the barrel prior to each experiment.

3.4 Dry and Wet Sand Experimental Set-up Used at Harvard

A careful procedure was developed for sample preparation and assembly to ensure that the compacted densities of each sand sample were well controlled and, for water saturated samples, to ensure complete saturation without trapped air and with no loss of water prior to the experiment. The samples were prepared with two sizes of sieved sand; Coarse samples had particle sizes of 425 to 500 μm, while fine sand ranged from 75 to 150 μm in size. The sand samples were contained in polycarbonate holders, machined to sufficient dimension to avoid observation of lateral release at the downrange sample surface. A metallic driver plate confined the sample at the rear (impact) surface to permit a symmetric impact with a flyer of identical composition (Cu). The downrange face of the sample was confined with an aluminized PMMA window. For all samples, it was critical to ensure uniform compaction of the sand grains from shot to shot so that the initial bulk densities would be comparable. For dry, coarse sand samples the maximum packing achievable was determined to be ~65% of the theoretical density while for the fine sand, it was ~64% of theoretical density, similar to that achieved in the Georgia Tech and Eglin experiments. These values were determined through compaction tests in samples that were not shot. Water saturated samples were designed to achieve the same compaction as the dry samples and masses were chosen to yield a 4.5mm thick sample at full compaction in all cases.

For the water-saturated samples, it was critical to ensure complete saturation and that no water was lost prior to the shot, including under vacuum. Excess water was added to the sample reservoir and it was gently stirred and tapped to free adhered bubbles, allowing them to float to the surface. The sand surface was then smoothed as much as possible and additional water was added to form a meniscus above the top of the polycarbonate reservoir. The PMMA window was then slowly hand-pressed to meet the top of the sand, squeezing out excess water. By overfilling the reservoir to form a meniscus, the window makes its first contact with the water at the center of the samples, ensuring that no air bubbles are trapped beneath the window as it is pressed into place. Following this, the windows were tapped into their final position using a press piston and a rubber-faced mallet. Optimal compaction of the sand and the desired sample thickness was verified by measuring the assembled target thickness. Similarly, the mass of each component was recorded during assembly so that the final mass of sand and water are individually known and can be compared to their calculated volumes. The windows were sealed with epoxy (the mass of which was also recorded) and left to cure overnight. The following day, the target assembly was weighed again to check for evaporative mass loss and then placed under vacuum in a bell jar for 1-2 hours to verify that there are no

leaks through which water could be lost during the experiment. Following this test, we again verified that the assembled target mass was unchanged, and hence the target remained saturated. Finally, samples were monitored for water loss in-situ using a capacitance probe in contact with the sample. This was monitored during evacuation of the target chamber and just prior to the shot. The combination of these measures allowed confidence that the samples are of well-characterized bulk density and remain saturated at the time of the experiment.

Figure 10 illustrates schematics and photographs of designs used for wet and dry sand targets used for performing uniaxial-strain planar parallel plate-impact experiments on the Harvard single-stage gas gun. Cu flyer plates were accelerated with compressed He or powder, and shock transit times were measured using piezo-electric pins on the uprange and downrange surface of the sample and with two channels of point VISAR.

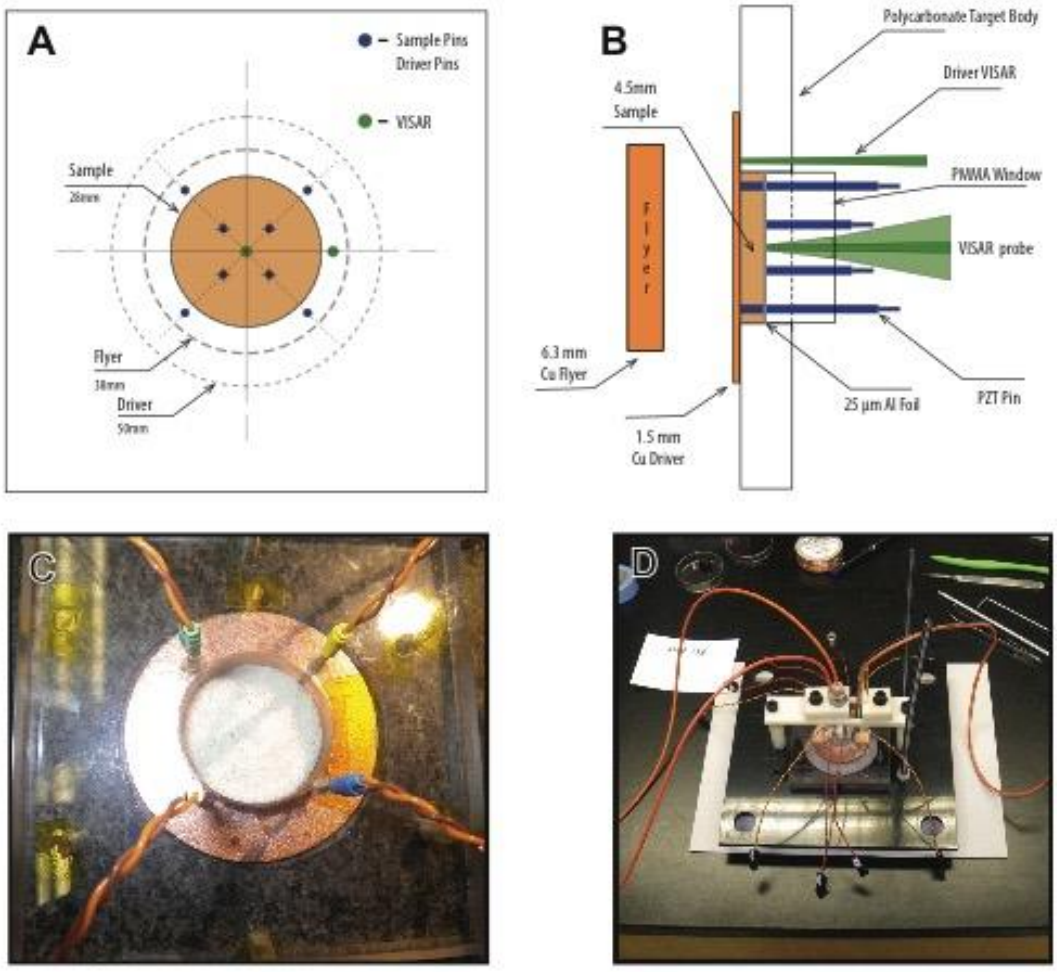

Figure 10. Designs used for wet and dry sand targets on Harvard single-stage gas gun. (A,B) Sand sample is contaned in polycarbonate holder with velocity measurements made at uprange and downrange target faces using piezo-electric pins and point VISAR. (C) The sample is shown before wetting the sand and inserting the PMMA window. (D) The assembled target, ready for mounting, with VISAR probes attached.

4 MESO-SCALE SIMULATIONS OF SHOCK RESPONSE OF SAND

4.1 Simulation Methodology and Validation

Mesoscale simulations using the Eulerian hydrocode CTH [7] were performed similar to previous works done by Benson [11], Vogler and Borg [9,10]. The approach aims to observe the macroscopic dynamic behavior of sand by resolving mesoscale attributes of the sand such as individual sand grains and porosity between grains. Three dimensional sand geometries were created by packing spheres into a sample domain that represented a portion of the experimental sand domain. The packing process was achieved by incrementally "growing" point masses (spherical grains) in a confined domain. Randomized final geometries were ensured by allowing grains to move with Brownian motion as they grow and come into contact with one another. Examples of final sand geometries uploaded into CTH are shown in Figure 11. Note that grains extend out of the lateral domain in order to utilize periodic boundary conditions, which is a common simulation technique used to represent an infinitely wide domain. These boundary conditions are particularly useful in cutting down the computational expensiveness of the simulations. Inflow and outflow conditions were specified at the inlet and outlet of the longitudinal direction. The resolution of the simulations was determined using 6 cppr (cells per particle radius), a commonly accepted resolution for these types of simulations [9,10].

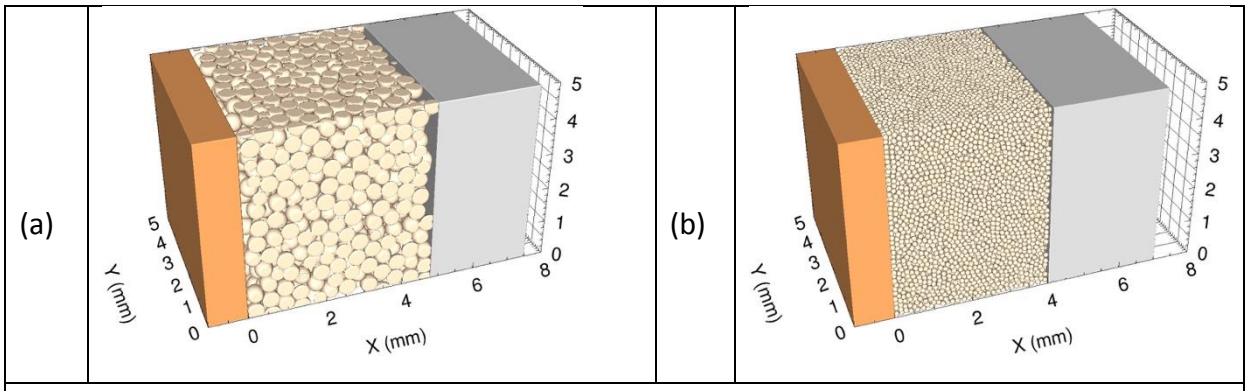

Figure. 11 Sand realization imported in CTH hydrocode (a) 433 µm and (b) 133 µm

As mentioned earlier, the mesoscale approach assigns homogeneous properties to individual heterogeneous features. Therefore, each grain of sand in the computational domain was treated as a sphere with pure crystalline quartz properties. The equation of state for crystalline quartz has historically been difficult to perfect due to significant variations in the behavior between different crystalline orientations, i.e. x-cut, y-cut, z-cut. Along with these differences, the elastic-plastic transition point (yield strength) has been shown to range from 4 to 12 GPa, and it is well known that a polymorphic phase transition exists at pressures around 40 GPa [12]. Due to its complexity, there is need for further development of an equation of state for quartz that will accurately depict one-dimensional homogeneous behavior as well as accurately yield the dynamic behavior of sand. In order to provide the individual sand grains with a Quartz equation of state, parameters were inferred from Wackerle's work on crystalline quartz [12]. The final parameters are listed in Table I.

Table I. Baseline materials and constitutive constants

Parameter	Quartz [12]	Copper [7]	PMMA [7]	Water [7]
Density, ρ (g/cm^3)	2.65	8.930	1.186	0.998
Sound speed, c_0 (km/s)	3.7784	3.940	2.300	1.48
Hugoniot Slope, s	2.12	1.489	1.750, -0.130	1.984,-0.143
Grüneisen Coefficient, $\Gamma = V(\partial P/\partial E)_V$	0.9	1.990	0.910	0.480
Specific Heat, C_V (J/g-K)	0.850	0.393	3.020	3.690
Dynamic Yield Strength, Y (GPa)	4.1	0.217	0.055	N/A
Poison Ratio, υ	0.15	0.335	0.35	N/A
Fracture Strength, σ_s (GPa)	5	0.338	0.085	N/A

The brittle nature of quartz and the unique stress load that each grain experiences in a sand sample makes the dynamic behavior difficult to accurately portray. Zbib et al [13] showed how grains simply pulverize under stress, which is extremely difficult to model, no matter the computational method. Once a grain has pulverized, its pieces fill void spaces in between other grains and this behavior can be lost in the models because their initial resolution is optimized to resolve the smallest feature in the domain; an individual sand grain. Once grains break into much smaller than an uncrushed grain, the pieces can get "washed out" within the domain. This is an inherent problem with Eulerian hydrocodes because fracture is not explicitly resolved. When a material in this type of calculation experiences a specified tensile stress, a void is introduced to relieve the stress; an intuitive albeit simplified strategy. In the present case a Von Mises, elastic-perfectly-plastic, strength model was used for Quartz, Copper, and PMMA.

Table II provides the characteristics of sand geometries created for CTH. Mono-dispersed grains were chosen for 'coarse' and 'fine' sand particles to simplify the geometries and remove an unknown in the overall modeling process. Also, the same bulk properties of quartz were given to every grain. Future work could expand on these assumptions to investigate the effect of using polydispersed grain distributions and size-dependent material properties.

Table II. Baseline material and constitutive constants

Geometry	Sand Vol. Frac.	Water Vol. Frac.	Dry Density (g cm^{-3})	Wet Density (g cm^{-3})
Coarse Dry (465 μm)	65	0	1.723	-
Fine Dry (150 μm)	64	0	1.720	-
Coarse Wet (465 μm)	65	35	1.720	2.070
Fine Dry (150 μm)	64	36	1.720	2.060

The macroscopic propagation of shock waves through granular materials is highly dependent on the grain contact networks or stress bridges that dictate how stress is passed from one grain to the next. Therefore, adequately representing contact interfaces between grains is crucial to capturing the underlying physics. In Eularian Hydrocodes such as CTH, the grain interfaces are not explicitly resolved, but rather defined using partially filled cells on the boundaries of each grain. Therefore, grain interactions are handled entirely through the communication of partially filled cells located on the perimeter of grains. Partially filled cells on grain interfaces require special treatment specifically when calculating stress because strength is what distinguishes these calculations from purely hydrodynamic simulations. Without strength, grains would flow similar to liquid as soon as they were impacted. When the perimeter of multiple grains overlap within a single computational cell, the strength of that cell can be calculated by either setting the cell strength to zero (refered to as 'mix 5') or calculating the strength based on a volume weighted average of each material's strength present in the cell. If the grains in contact share the same material number, they will essentially be "welded" together because that cell will not be able to distinguish the grain boundary. In order to prevent welding (stiction), neighboring grains are assigned different material numbers, but the same material properties. Therefore, grain interfaces can be inferred from cells that contain mass from multiple material numbers and, further, some level of grain contact can be controlled.

The 'mix 5' option, which sets the strength of partially filled cells to zero, results in a thin layer of liquid surrounding each grain. This liquid layer results in a large portion of the overall sand domain having zero strength and the grains subsequently "snowplow" when compacted. Such a behavior can be observed in the pressure-density Hugoniot plots for simulations using the 'mix 5' option, as will be presented later. The volume weighted option for mixed cells (refered to as 'mix 3'), yields a much more physically sound calculation because the strength on grain perimeters is maintained to a degree. However, strength on perimeter cells is still much different than actually incorporating Coloumb friction at particle interfaces. Extensive work has been done by Borg and Volger [9,10] to characterize the components of *slide* and *stiction* mechanisms in CTH. Their work concluded that allowing grains to *slide* yielded a much more accurate result in terms of matching experimental data on granular media. Therefore, the *slide* option was used in all of the present CTH simulations.

Experimental particle velocity profiles were recreated in CTH by placing a uniformly distributed plane of 100 tracer points across the sand-PMMA interface. In order to capture a more continuum or average response of the sand, the plane of tracers was chosen to cover the majority of the interface. Therefore, it spanned 4.05 mm x 4.05 mm in the y and z direction yielding a square area of approximately 16 mm^2, which is comparable to the area covered by a Manganin stress gauge. The heterogeneous nature of sand disrupts planar shock propagation during dynamic loading, which can be observed using these multiple tracers. Since a VISAR laser spot collects data across the size of roughly one sand grain, the observed particle velocity profile is highly dependent on the local grain realization near the sand-PMMA interface. Using multiple tracers across the interface allows for velocity profiles to be measured near multiple local grain realizations. It also allows for a continuum or average response to be calculated, and ultimately helps display the dispersion of the shock front as a result of different size sand grains. A plane of tracers was placed at the copper-sand interface, as well as the sand-PMMA interface in order to accurately calculated transit time within the sand sample.

4.2 Correlations with experimental Results

Both coarse and fine sand grain samples followed a linear trend in U_s-U_p Hugoniot space with little difference visible between coarse and fine grain samples. Likewise, water saturated sand samples for both coarse and fine grains seem to follow similar U_s-u_p Hugoniots. Fitting the data in Figure 12b provided the Hugoniot relationships for each of the sand samples, Table III.

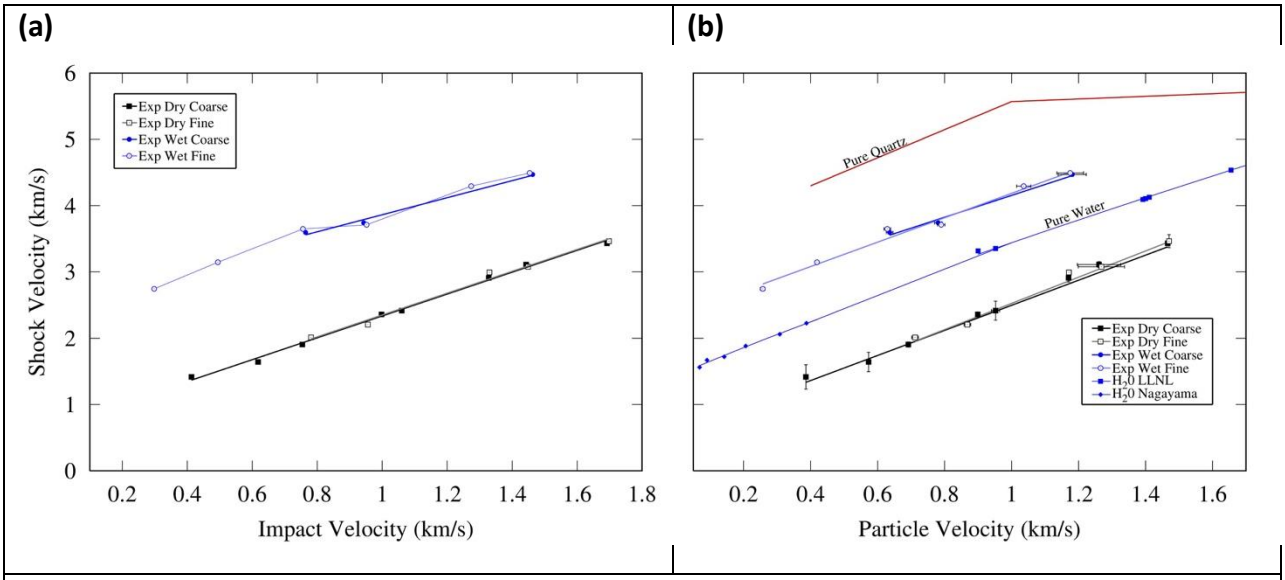

Figure. 12. (a) Shock velocity vs Impact Velocity (b) Shock Velocity vs Particle Velocity including sound speed measurements

Table III. U_s-u_p Hugoniots for the four sand samples

Coarse Dry	$U_s = 1.962u_p + 0.548$
Fine Dry	$U_s = 2.000u_p + 0.555$
Coarse Wet	$U_s = 1.649u_p + 2.505$
Fine Wet	$U_s = 1.840u_p + 2.345$

Figure 13 shows a comparison of the three-dimensional CTH simulated shock response with the experimental data. It can be observed that the simulations provide an upper and lower bound on the experimental data. The upper bound being with simulations that used the volume weighted mixed cell strength, 'mix 3', and the lower bound being simulations that treated mixed cells with zero strength, 'mix 5'. Interestingly, around a particle velocity of roughly 0.9 km/s, simulations using 'mix 3' and simulations using 'mix 5' converge onto the experimental data. This trend holds for both coarse and fine sand simulations. The over prediction of shock velocity for volume weighted calculations in the lower particle velocity region suggests that too much strength is given to grain interfaces and the rigid contact allows stress waves to easily propagate with minimal losses. The under prediction of setting partially filled cells to zero strength depicts the snowplow behavior mentioned earlier.

Shockwaves traveling in actual sand samples experience significant losses due to many mesoscale mechanisms that disable paths for stress waves to travel. However, above a certain stress loading magnitude, the initially porous sand now has most of its porosity crushed out, the homogeneous quartz that makes up individual grains is behaving hydrodynamically, and the macroscopic response of the sand approaches that of pure quartz. In this regime many mesoscale mechanisms that limit the physical accuracy of the simulations become less of a factor. The lower end of this region can be observed in Figure 13 where simulations for either mixed cell strength calculation converge onto the experimental data. The point at which this happens in the simulations is thought to occur when cell values for stress reach that of the specified yield strength for quartz. Therefore, by changing the yield strength of pure quartz, i.e. the properties of the bulk homogeneous material, the simulated dynamic response of sand can be controlled.

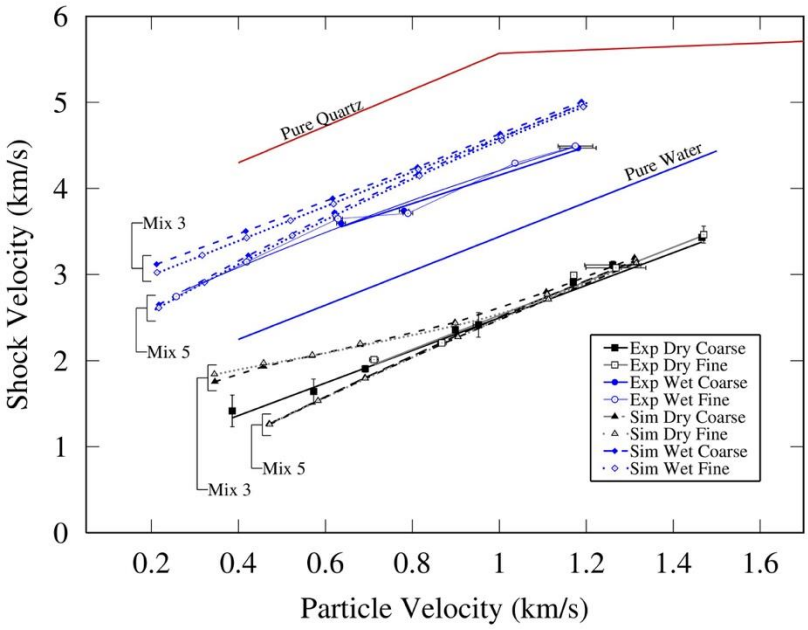

Figure 13. Simulated shock response compared to experimental data.

The shock state Hugoniot pressure was calculated from the Rankine Hugoniot jump equation

$$P_H = \rho_0 U_s u_H \quad (1)$$

where ρ_0 is the initial density of the sand, U_s is the shock velocity, and u_H is the particle velocity within the sand. The impedance matching technique used to find u_H is described in the calculations section. Figure 14a shows the pressure versus particle velocity curves for both the experimental and simulated results. The upper and lower bounds made by the simulations are slightly more difficult to observe in this space. However, it can be seen in Figure 14a that the convergence around 1 km s^{-1} occurs at approximately 5 GPa, slightly above the yield strength specified for quartz in the simulations. Figure 14b shows the release or reshock behavior observed at the sand-PMMA interface. This state is inferred from the VISAR profiles experimentally and from the spatially averaged tracer profiles computationally. To calculate pressure at the sand-PMMA interface, the Hugoniot for PMMA was used.

$$P_R = \rho_0 u_R (s_1 u_R^2 + s_2 u_R + c_0) \quad (2)$$

In equation (2), P_R is the release or reshock pressure at the sand-PMMA interface, u_R is the release or reshock velocity, s_1 and s_2 are Hugoniot fit parameters for PMMA, and c_0 is the bulk sound speed of PMMA. Since the impedance of dry sand is close to, but less than that of PMMA, the sand actually reshocks to a higher state when the wave reaches the sand-PMMA interface. This reshock behavior lasts until approximately 6 GPa where the dry sand Hugoniot becomes greater than that of PMMA and the sand then releases stress when the wave reaches the PMMA window. In either case, the similar impedance of dry sand and PMMA make it

difficult to draw conclusions about how the sand either releases or reshocks after being loaded. Conversely, the impedance of fully saturated sand is much higher than that of PMMA which makes information about the release more available. Even though the saturated sand is not allowed to fully release, the difference in pressure between the Hugoniot state and the release state are adequate enough to infer characteristics of the release path. Prior work by Braithwaite et al has shown that the full release path for sand can be approximated as linear [14]. Therefore, the partial release path for the current work was approximated to be linear as well. As figure 14b shows, the release path of the saturated sand lies on or slightly below the Rayleigh loading line. Therefore, the shock-release process is approximately elastic.

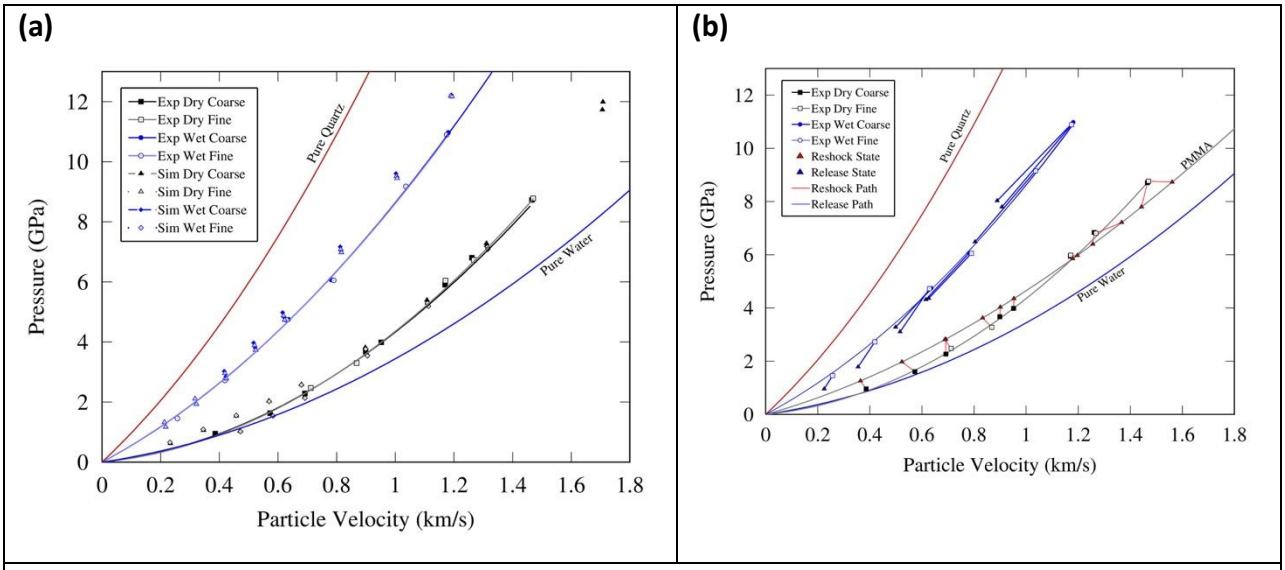

Figure 14. Pressure vs Particle Velocity (a) experimental and simulated Data (b) experimental data with reshock/release paths. Red lines indicate reshock and blue lines indicate release

The release paths for each of the simulations were also calculated and are compared to the experimental paths in Figure 15, below. It can be observed from Figure 15 that the simulation release paths, for both coarse and fine grain sand, reveal much more irreversibility than the experiments. The two different mixed cell strength calculations, ‘mix 3’ and ‘mix 5’, also show noticeable differences. Volume weighted mixed cell strength, ‘mix 3’, release paths appear to follow the Rayleigh loading line more closely; a behavior more prominent in coarse grain simulations.

The snowplow artifact of setting cells with mixed cell strength to zero, ‘mix 5’, reveals itself in release paths more representative of inelastic loading cycles. The difference between the two could be attributed to the large amounts of zero strength material in ‘mix 3’ simulations that don’t allow grain boundaries to be maintained. Grain deformation, i.e. strain, is a large factor in the reversibility of the loading cycle.

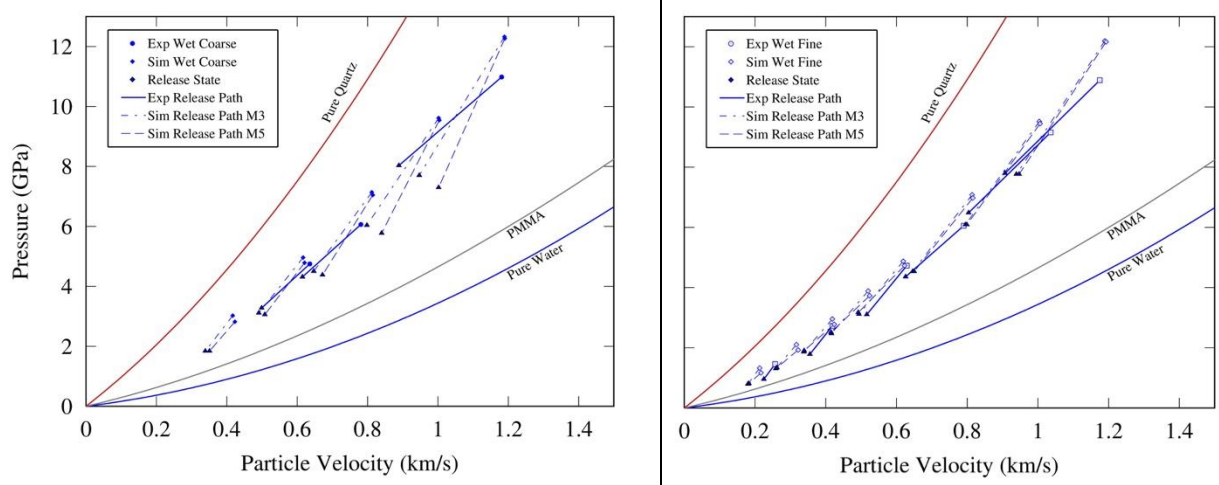

Figure 15. Experimental and simulated release paths (a) coarse grain sand (b) fine grain sand.

Hugoniot density was also calculated from the jump equations as

$$\rho_H = \frac{\rho_0 U_s}{U_s - u_H} \quad (3)$$

where ρ_H is the density of sand at the Hugoniot state. Figure 16 compares the simulations to the experiments as well as shows release and reshock data for the experiments. The Hugoniot for dry sand initially shows large amounts of compression and then stiffens up as it approaches the pure quartz Hugoniot.

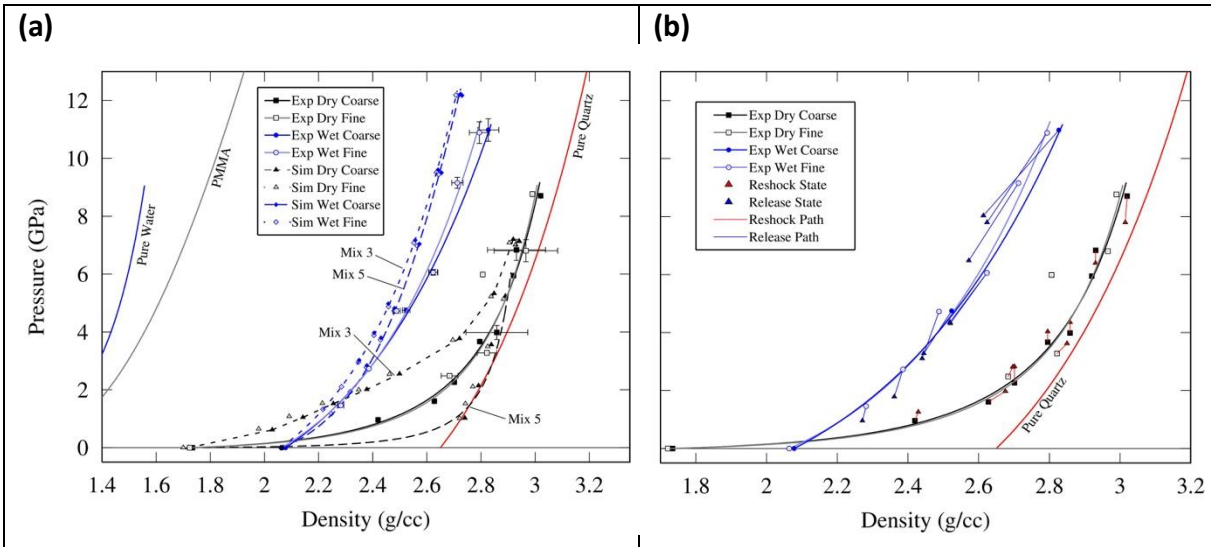

Figure 16. Pressure vs Density (a) experimental and simulated data (b) experimental data with reshock/release paths.

The reshock or release points shown in Figure 16b above were calculated based on analysis done by Brown et al where the final state at the PMMA window is assumed to be an "off-Hugoniot" state [4]. Shock velocity in the Lagrangian reference frame is given by

$$U_{sR} = \frac{P_R - P_H}{\rho_0 (u_H - u_R)} \quad (4)$$

where P_R is the release/reshock pressure defined earlier. The off-Hugoniot density is then calculated as

$$\rho_R = \rho_0 \left(\frac{\rho_0}{\rho_H} - \frac{u_H - u_R}{U_{sR}} \right)^{-1} \quad (5)$$

The off-Hugoniot or release/reshock density and pressure are presented in Figure 16b (above) for the experimental data and in Figure 17 (below) for comparisons between experiments and simulations. It should be noted that near the point at which the dry sand Hugoniots for coarse and fine sand intersect that of PMMA, the equation for off-Hugoniot density breaks down asymptotically. Therefore, the release/reshock path for three dry - fine sand data points and one coarse sand data point were discarded. Regardless, Figure 7 also shows that the simulated results for saturated sand ware less elastic and that giving the surfaces of grains zero strength results in significantly larger amounts of irreversibility. This supports the idea that the strength of mixed material cells located on grain interfaces must me accounted for in order to more accurately reproduce experimental results as well as maintain a more physically representative model for the sand.

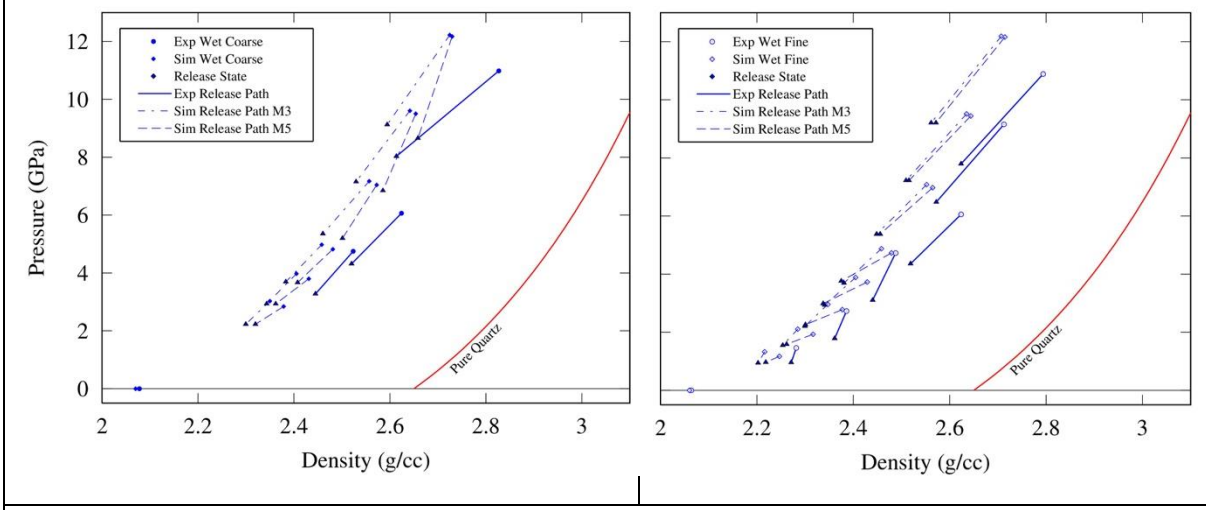

Figure 17. Experimental and simulated release paths (a) coarse grain sand (b) fine grain sand.

4.3 Calculations and Error Analysis

In order to calculate the shock velocity, the sample thickness was divided by the transit time. Each of the velocity profiles measured using VISAR from the sample-PMMA interface were time shifted such that the arrival of the shock wave at the back of the driver plate signified time equal to zero. Transit time was determined by locating the point at which the particle velocity ramp had reach 50% of its overall plateau. Additionally, the point at which 10% and 90% of the particle velocity plateau was achieved was used to calculate the rise time. Figures 18a and 18b show examples of the three time of arrival points, t_{10}, t_{50}, t_{90}, for two particle velocity profiles.

Figure 18a shows a simulated particle velocity profile that is calculated from an average of 100 tracer points spread laterally across the sand-PMMA interface. Figure 18b is an experimental particle velocity profile measured using VISAR (shot h140).

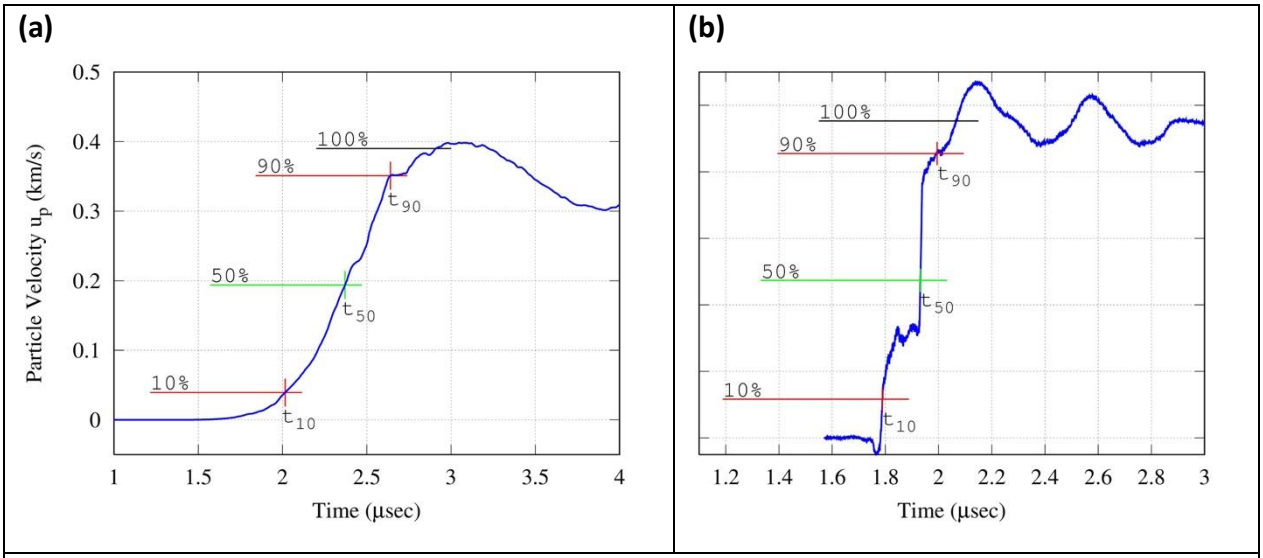

Figure 18. Particle velocity profiles depicting the location of 10%, 50%, 90%, and 100% of the particle velocity profile, u_p, and the corresponding times t_{10}, t_{50}, t_{90}. (a) CTH simulation u_0 = 500 m/s. (b) Experimental measurement using VISAR (h140) u_0 = 943 m/s. Both results are for dry, coarse sand.

Shock or ramp velocity can then be calculated as the sample thickness, dx, divided by the transit time, dt, or

$$U_s = \frac{dx}{dt} = \frac{dx}{t_{50}}. \quad (6)$$

Impedance matching was done to find the particle velocity inside the sand sample:

$$u_p = \frac{-B - \sqrt{B^2 - 4AC}}{2A}. \quad (7)$$

where:

$A = s_{cu}$	(8)
$B = 2s_{cu}u_0 + c_{cu} + \frac{\rho_{sand}}{\rho_{cu}}U_s$	(9)
$C = c_{cu}u_0 + s_{cu}{u_0}^2$	(10)

or in expanded form:

$u_p = \frac{-2s_{cu}u_0 + c_{cu} + \frac{\rho_{sand}}{\rho_{cu}}U_s - \sqrt{\left(2s_{cu}u_0 + c_{cu} + \frac{\rho_{sand}}{\rho_{cu}}U_s\right)^2 - 4s_{cu}(c_{cu}u_0 + s_{cu}{u_0}^2)}}{2s_{cu}}$	(11)

The goal of this section is to propagate experimental errors for U_s, u_p, ρ_H, and P_H. Below are the independent variables used when calculating shock velocity and their sources of uncertainty.

Table IV. Independent Variables for Shock Velocity U_s

Variable	Source of Uncertainty
Sand Sample Thickness (x)	• Measurement uncertainty
Transit Time (t) (Measured from 50% of driver rise to 50% of sample rise)	• Uncertainty from tilt correction • Rise time at Cu-Sand interface • Rise time at Sand-PMMA interface

The main difficulty here is quantifying uncertainty for transit time. As a first pass to quantify uncertainty in transit time, the half rise time at the driver and the half rise time at the sand-PMMA interface were used as the uncertainty in the total amount of time it took for the wave to go from the driver-sand interface to the sand-PMMA interface. The transit time is defined as

$t = t_{50} - t_0$	(12)

where t_{50} is the time at which the sand-PMMA interface has reached half the up plateau and t_0 is the time at which the driver up has reached half its plateau. Therefore, uncertainty in transit time is given by

$$\delta t = \sqrt{(\delta t_{50})^2 + (\delta t_0)^2} = \sqrt{\left(\frac{t_{90} - t_{10}}{2}\right)^2_{driver} + \left(\frac{t_{90} - t_{10}}{2}\right)^2_{sample}}. \quad (13)$$

Once the uncertainties for sample thickness and transit time have been specified, the propagated uncertainty for shock velocity is given as:

$$\delta U_s = \sqrt{\left(\frac{\partial U_s}{\partial x}\delta_x\right)^2 + \left(\frac{\partial U_s}{\partial t}\delta_t\right)^2}. \quad (14)$$

Additional uncertainty was considered for the tilt correction; however, its uncertainty value was approximately 5 ns so it was neglected. Further work could be done to incorporate error resulting from the aluminum layer/gage layer at the interface, but it is assumed to be incorporated within the current half rise time approach. Next, the uncertainty in particle velocity as a result of the impedance matching technique was calculated.

Table V Independent Variables for Particle Velocity u_p

Variable	Source of Uncertainty
Shock Velocity (Us)	• Uncertainty carried over from δU_s
Impact Velocity (u_0)	• Measurement uncertainty
Sand Density (ρ_s)	• Measurement uncertainty
Copper Density (ρ_c)	• Measurement uncertainty
Copper Hugoniot Slope (s)	• Estimate 5% of value
Copper Bulk Sound Speed (C)	• Estimate 5% of value

Most of the uncertainty in particle velocity is incurred from shock velocity, measurement uncertainty in impact velocity, sand density, copper density, and then general uncertainties in the Hugoniot fit parameters for Copper. The uncertainty in particle velocity was calculated as follows

$$\delta U_p = \sqrt{\left(\frac{\partial u_p}{\partial U_s}\delta_{U_s}\right)^2 + \left(\frac{\partial u_p}{\partial u_0}\delta_{u_0}\right)^2 + \left(\frac{\partial u_p}{\partial \rho_s}\delta_{\rho_s}\right)^2 + \left(\frac{\partial u_p}{\partial \rho_c}\delta_{\rho_c}\right)^2 + \left(\frac{\partial u_p}{\partial s}\delta_s\right)^2 + \left(\frac{\partial u_p}{\partial c}\delta_c\right)^2}. \quad (15)$$

Error bars for Hugoniot pressure were calculated using a similar error propagation technique as outlined for shock and particle velocity. Hugoniot pressure is dependent on three variables, namely, initial density of the sand, shock velocity, and particle velocity. The uncertainty in density is a measurement uncertainty and the uncertainty for shock velocity and particle velocity are carried over. The general form of uncertainty in Hugoniot pressure is then,

$$\delta P = \sqrt{\left(\frac{\partial P}{\partial \rho_s}\delta\rho_s\right)^2 + \left(\frac{\partial P}{\partial U_s}\delta U_s\right)^2 + \left(\frac{\partial P}{\partial u_p}\delta u_p\right)^2}$$	(16)
$$= \sqrt{\left(U_s u_p \delta\rho_s\right)^2 + \left(\rho_s u_p \delta U_s\right)^2 + \left(\rho_s U_s \delta u_p\right)^2}.$$	(17)

The calculation of uncertainty in Hugoniot density is a similar process to that for Hugoniot pressure since Hugoniot density is dependent on the same three variables as pressure. Therefore, uncertainty in Hugoniot density has the form

$$\delta\rho = \sqrt{\left(\frac{\partial \rho}{\partial \rho_s}\delta\rho_s\right)^2 + \left(\frac{\partial \rho}{\partial U_s}\delta U_s\right)^2 + \left(\frac{\partial \rho}{\partial u_p}\delta u_p\right)^2}$$	(18)
$$= \sqrt{\left(\frac{U_s}{U_s - u_p}\delta\rho_s\right)^2 + \left(\frac{\rho_s u_p}{\left(U_s - u_p\right)^2}\delta U_s\right)^2 + \left(\frac{\rho_s U_s}{\left(U_s - u_p\right)^2}\delta u_p\right)^2}.$$	(19)

Table VI. Experimental data for both grain sizes and saturations

Shot	Grain Diameter (μm)	Saturation (%)	Density (g cm^{-3})	Impact Velocity (m s^{-1})	Particle Velocity (m s^{-1})	Shock Velocity (m s^{-1})
GT1338	450-500	0	1.760	413	386	1416
GT1335	450-500	0	1.710	618	573	1641
GT1337	450-500	0	1.720	754	692	1905
GT1336	450-500	0	1.730	998	899	2359
H140	450-500	0	1.732	1060	952	2416
E1433	450-500	0	1.746	1328	1170	2910
H141	450-500	0	1.743	1443	1261	3111
E1436	450-500	0	1.730	1692	1466	3432
H146	75-150	0	1.734	781	712	2012
H144	75-150	0	1.711	956	868	2205
E1330	75-150	0	1.708	1330	1171	2992
H145	75-150	0	1.744	1449	1268	3078
E1435	75-150	0	1.721	1698	1470	3464
H164	450-500	100	2.077	764	781	3595
H156	450-500	100	2.076	943	1181	3740
H155	450-500	100	2.080	1463	636	4470
H166	75-150	100	2.068	298	257	2744
H167	75-150	100	2.067	494	419	3145
H165	75-150	100	2.059	756	629	3649
H158	75-150	100	2.065	952	790	3711
H168	75-150	100	2.058	1274	1036	4293
H156	75-150	100	2.063	1454	1175	4492

5. SUMMARY, CONCLUSIONS, AND FUTURE WORK

5.1 Summary of Results

The purpose of this work was to observe characteristics of shock wave propagation in high purity sand of fine (75-150 μm) and coarse (425-500 μm) sizes in wet and dry conditions. The final bulk density of dry and wet sand was 1.72 g cm^{-3} and 2.02 g cm^{-3}, respectively, which corresponded to packed densities of about 65% quartz sand and 35% void space or water. The saturated samples were assumed to have no remaining void space once water was added in order to limit the system to a two-phase mixture. Uniaxial-strain plate-impact experiments were performed to compress these sands to pressures ranging from 1 - 9 GPa, corresponding to impact velocities of 0.2 to 2.0 km s^{-1}, using gas and powder guns at Harvard, Georgia Institute of Technology, and Eglin Air Force Base. Shock Hugoniots for the different sands were determined using impedance matching, which relied on shock velocity values calculated from sample thickness and time of arrival data collected by piezoelectric pins and particle velocity profiles measured using VISAR and PDV.

In conjunction with experimental work, mesoscale hydrocode simulations were performed using CTH to further validate current physical models and expand the general knowledge of sand's dynamic behavior. Mesoscale features of the sand were resolved by explicitly incorporating three-dimensional grains and void space into the computational domain. The bulk macroscopic response was observed using planes of tracer particles located at the buffer-sand interface as well as the sand-window interface. The plane of tracers at the sand-window interface allowed the experimental VISAR and PDV measurements to be recreated computationally with reasonable agreement. From transit time and sample thickness, shock velocity was calculated and impedance matching was then performed to obtain all other state variables.

Considering the bulk propagation of waves through sand is highly dictated by grain contact networks, the treatment of those interface points is crucial in achieving accurate simulation results. Therefore, much effort was spent controlling the contact mechanisms between grains such as friction and material strength. Effects of grain-on-grain interaction was explored within CTH by ((A) altering the scheme in which material yield strength was determined at grain interfaces) ((B) varying the yield strength of computational cells located at the interface of grains) and observing the overall macroscopic result. The two options for determining the value of material strength in cells at grain interfaces were to set the cell strength to zero, 'mix 5', or to use a volume averaged yield strength, 'mix 3.'

5.2 Conclusions

Dry sand Hugoniots for both coarse and fine grain sand followed a linear trend, similar to the results of other works on dry sand [4, 14]. Interesting to note is the lack of difference between fine and coarse grain Hugoniots. Even though the Hugoniots are similar, it does not provide insight into how different size grains the distribute stress within the compressed sand sample. Hugoniots for the simulations and experiments show that the two mixed cell yield strength options provided by CTH form an upper and lower bound on the experimental data; 'mix 3' providing an upper bound and 'mix 5' providing a lower bound. The fact that 'mix 5', zero strength at grain interfaces, agrees fairly well at lower velocities suggests that the mix3, volume weighted mixed cell strength, option does not capture many of the mesocopic effects that can slow down the bulk propagation of stress waves in heterogeneous materials. Although the hydrodynamic treatment of grain interface/surface cells in the 'mix 5' simulations is highly non-physical, it suggests that effects such as microkinetic energy, chipping on grain surfaces, and plastic deformation are highly present in experimental tests because the implication of hydrodynamic grain surfaces means grains will slide by one another more easily as a result of plastic flow, chipping, and lack of friction. Therefore, more energy will be absorbed in compacting the grains instead of propagating stress waves through grain contact points. Essentially, experimental test results show a significant reduction in bulk wave speed and in order to accurately simulate such a phenomenon, multiple complicated mechanisms need to be implemented in some form or another.

5.3 Future Work

The experimental Hugoniot for fine and coarse saturated sand appear to have overall linear trend lines, however, an inflection point near 4.5-6 GPa and 0.6-0.8 kms^{-1} in the fine grain saturated sand Hugoniot could be inferred and expanded upon in future work. Various mechanisms could potentially be at play such as phase transition of Quartz to Coesite and shock-induced ice formation in water. Further Hugoniot points for fine saturated sand would need to be added in order to support these hypotheses, as well as additional Hugoniot points for coarse saturated sand to test if this inflection point is present for multiple grain sizes. From a computational perspective, additional effort should be placed into modifying the quartz equation of state to incorporate phase change seeing as this could be a source for this inflection point in the saturated fine Hugoniot. More fundamental, the implementation of friction and fracture mechanisms in any simulation are necessary to obtaining a more physically representative result that agrees with experimental data.

6. GRADUATE EDUCATION AND RESEARCH TRAINING

In addition to the co-PIs Naresh Thadhani and Sunil Dwivedi at Georgia Tech, Sarah Stewart at Harvard University, and John Borg at Marquette University, the students and research scientists participating in this project and supported under the current grant are listed in Table I. The graduate students from Marquette who worked on the modeling efforts visited Georgia Tech to participate in the experiments and gain better understanding of the experimental results. The students and research scientists from Marquette and Goergia Tech also participated in the experiments performed at AFRL, Eglin AFB, as well as to be aware of the areas of interest to DoD and to establish collaborative ties with AFRL researchers.

Table VII: Students and Research Scientists Supported under AFOSR Grant

Name (Institution)	**Degree Sought**	**Grad. Date**
David Scripka (GaTech)	Ph.D. – Materials Science & Engineering	May 2017
Andrey Kossev (GaTech)	B.S. – Materials Science & Engineering	May 2015
Julien Turner (Georgia Tech)	B.S. – Materials Science & Engineering	May 2014
Greg Kennedy (GaTech)	Research Scientist	
Rick Kraus (Harvard Univ)	Ph.D. – Planetary Physics	June 2013
Matt Newman (Harvard Univ)	Ph.D. - Planetary Physics	June 2013
Dylan Spaulding (Harvard University)	Post-doc	
Jeff Lajeunesse (Marquette)	Master of Science - Mech. Engineering PhD - Mech. Engineering	May 2015 Exp. May 2018
Merit Schumaker (Marquette)	Master of Science - Mech. Engineering	May 2015

7. PRESENTATIONS AND PUBLICATIONS

- LaJeunesse, J., Schumaker, M., Stewart, S., Borg, J., Resolving the Dynamic Response of Sand, Annual International Workshop on Dynamic Behaviour of Structures and Materials, Interaction and Friction Across the Strain Rates 2015, Abs.
- LaJeunesse, J., J. Borg, S. Stewart, N. Thadhani, Investigating Velocity Spectra at the Hugoniot State of Shock Loaded Heterogeneous Materials, *19th APS Topical Conference on Shock Compression of Condensed Matter*, Abs. U6.00002, 2015.
- LaJeunesse, J., Borg, J., Martin, B., Simulating the Planar Shock Response of Concrete, Society for Experimental Mechanics, Dynamic Behavior of Materials, 2014, Conference Proceedings
- Schumaker, M., S. T. Stewart, J. P. Borg, Stress and Temperature Distributions of Individual Particles in a Shock Wave Propagating through Dry and Wet Sand Mixtures, *19th APS Topical Conference on Shock Compression of Condensed Matter*, Abs. L6.00006, 2015.
- Schumaker, M., Borg, J., Kennedy, G., Thadhani, N., Mesoscale simulations of Dry Sand, Society for Experimental Mechanics, Dynamic Behavior of Materials, 2014, Conference Proceedings
- Newman, M., S. Stewart, R. Kraus, Hugoniot Measurements on Dry and Water-Saturated Soils, *19th APS Topical Conference on Shock Compression of Condensed Matter*, Abs. L6.00005, 2015.
- Kennedy, G., Thadhani, N.N., Markos, H., Stewart, S., Neel, C., Dynamic high pressure behaviopr of Quartz Silica Sand of two different particle sizes, *APS Topical Conference on Shock Compression of Condensed Matter*, Abs. L6.00002, 2015.

8. ACKNOWLEDGEMENTS

The authors sincerely acknowledge the funding provided by the AFOSR under Award No. FA9550-12-1-0128, with Dr. Jonnifer Jordan as the program monitor. The support of Dr. Kit Neel, and his team at the Air Force Research Laboratory at Eglin Air Force Base, is also acknowledged for their support in conducting the experiments. Finally, the U.S. Army Engineering Research and Development Center (ERDC) DoD Supercomputing Resource Center (DSRC) is acknowledged for the allocation on the time for performing the computational simulations.

9. BIBLIOGRAPHY

1. Anderson, G. D., G. E. Duvall, J. O. Erkman, G. R. Fowles, and C. P. Peltzer (1966), Investigation of eqution of state of porous earth media, Technical Report AFWL-TR-65-146, 176 pp, SRI Int., Menlo Park, CA.

2. Al'tshuler, L. V., and M. N. Pavlovskii (1971), Response of clay and clay shale to heavy dynamic loading, Journal of Applied Mechanics and Technical Physics, 1, 161-165.

3. Borg, J. P., D. J. Chapman, K. Tsembelis, W. G. Proud, and J. R. Cogar (2005), Dynamic compaction of porous silica powder, J. Appl. Phys., 98 (7), 073509, doi:10.1063/1.2064315.

4. Brown, J. L., T. J. Vogler, D. E. Grady, W. D. Reinhardt, L. C. Chhabildas, and T. F. Thornhill (2007), Dynamic Compaction of Sand, in Shock Compression of Condensed Matter -- 2007, edited by M. Elert, et al., pp. 1363-1366, AIP, Melville, NY.

5. Chapman, D. J., C. H. Braithwaite, and W. G. Proud (2007), Shock-loading of statically compacted soil, in Shock Compression of Condensed Matter -- 2007, edited by M. Elert, et al., pp. 1367-1370, AIP, Melville, NY.

6. Barker, L. M. (1971), A Model for Stress Wave Propagation in Composite Materials, Journal of Composite Materials, 5, 10.1177/002199837100500202.

7. Stewart, S. T., A. Seifter, and A. W. Obst (2008), Shocked H2O Ice: Thermal Emission Measurements and the Criteria for Phase Changes during Impact Events, Geophys. Res. Lett., 35, L23203, doi:10.1029/2008GL035947.

8. Kraus, R. G., S. T. Stewart, A. Seifter, and A. W. Obst (2010), Shock and Post-shock Temperatures in an Ice-Quartz Mixture: Implications for Melting during Planetary Impact Events, Earth Planet. Sci. Lett., 289, 162-170, doi:10.1016/j.epsl.2009.11.002.

9. Borg, J and Vogler, T, Rapid Compaction of Granular Material: Characterizing Two and Three-Dimensional Mesoscale Simulations (under preparation).

10. Borg, JP and Vogler, TJ, The Effect of Water Content on the Shock Compaction of Sand, in DYMAT 2009, pp. 1545-1552

11. Benson, D. J., “High-pressure shock compression of solids IV: response of highly porous solids to shock loading, edited by L. Davison, Y. Horie, and M. Shahinpoor (Spring-Verlag, NY, 1997), pp. 233-255.

12. Wackerle, J., “Shock compression of quartz”, J. Appl. Phys. **33**, 922 (1962); http://dx.doi.org/10.1063/1.1777192

13. Zbib, M. B., Parab, N. D., Chen, W. W., Bahr, D. F., “New pulverization parameter derived from indentation and dynamic compression of brittle microspheres”, Powder Technology, doi:10.1016/j.powtec.2015.04.066

14. Braithwaite, C. H., Perry, J. I., Taylor, N. E., Jardine, A. P., Behaviour of sand during release from a shocked state, Applied Physics Letters 103, 154103 (2013); doi: 10.1063/1.4824764

1.

1. Report Type

Final Report

Primary Contact E-mail

Contact email if there is a problem with the report.

naresh.thadhani@mse.gatech.edu

Primary Contact Phone Number

Contact phone number if there is a problem with the report

404-894-2651

Organization / Institution name

Georgia Tech Research COrportion

Grant/Contract Title

The full title of the funded effort.

Dynamic High-Pressure Behavior of Hierarchical Heterogeneous Geological Materials

Grant/Contract Number

AFOSR assigned control number. It must begin with "FA9550" or "F49620" or "FA2386".

FA9550-12-1-0128

Principal Investigator Name

The full name of the principal investigator on the grant or contract.

Naresh Thadhani

Program Manager

The AFOSR Program Manager currently assigned to the award

Jennifer Jordan

Reporting Period Start Date

04/01/2012

Reporting Period End Date

12/31/2015

Abstract

The characteristics of shock-wave propagation in high purity sand of fine (75-150 μm) and coarse (425-500 μm) particle sizes in dry conditions at ~65% theoretical density, and water-saturated conditions with 35% void space filled with water, were collaboratively investigated, via controlled uniaxial-strain experiments and meso-scale modelling using CTH. The meso-scale features of the sand were resolved by explicitly incorpoprating 3D grains and void space into the computational domain. The methodology involved characterizing the structure and configuration of sand, as a model granular geological material, and explicitly tracking the effects of evolving material heterogeneities and their interactions with shock waves. It was observed that both dry and wet sand follow linear trends, with little difference in overall response between the two sizes of sand particles. Accounting for different strength values into CTH, provided upper and lower bounds to the experimental data. Results suggest effects of microkinetic energy, chipping on grain surfaces, and plastic deformation dominating the experimental response. These are difficult to incorporate in the simulation models. Experiments also reveal significant reduction in bulk wave speeds, which requires incorporation of multiple mechanisms in the simulations.

Distribution Statement

This is block 12 on the SF298 form.

Distribution A - Approved for Public Release

Explanation for Distribution Statement

If this is not approved for public release, please provide a short explanation. E.g., contains proprietary information.

SF298 Form

Please attach your SF298 form. A blank SF298 can be found here. Please do not password protect or secure the PDF The maximum file size for an SF298 is 50MB.

StandardForm298-AFOSRFinalReport.pdf

Upload the Report Document. File must be a PDF. Please do not password protect or secure the PDF . The maximum file size for the Report Document is 50MB.

AFOSR-SandFinalReport-30Mar2016.pdf

Upload a Report Document, if any. The maximum file size for the Report Document is 50MB.

Archival Publications (published) during reporting period:

Changes in research objectives (if any):

Change in AFOSR Program Manager, if any:

Extensions granted or milestones slipped, if any:

March 31, 2015 to December 31, 2015

AFOSR LRIR Number

LRIR Title

Reporting Period

Laboratory Task Manager

Program Officer

Research Objectives

Technical Summary

Funding Summary by Cost Category (by FY, $K)

	Starting FY	FY+1	FY+2
Salary			
Equipment/Facilities			
Supplies			
Total			

Report Document

Report Document - Text Analysis

Report Document - Text Analysis

Appendix Documents

2. Thank You

E-mail user

Mar 30, 2016 19:06:43 Success: Email Sent to: naresh.thadhani@mse.gatech.edu